

# Gravitational waveforms from periodic orbits around a charged black hole with scalar hair\*

Weike Deng (邓为可)<sup>1,2,3</sup>  Sheng Long (龙胜)<sup>4</sup>  Tan Qin (谭钦)<sup>2†</sup>  Jiliang Jing (荆继良)<sup>2‡</sup> 

<sup>1</sup>School of Science, Hunan Institute of Technology, Hengyang 421002, China

<sup>2</sup>Department of Physics, Key Laboratory of Low Dimensional Quantum Structures and Quantum Control of Ministry of Education, and Synergetic Innovation Center for Quantum Effects and Applications, Hunan Normal University, Changsha 410081, China

<sup>3</sup>Hengyang Vocational College of Science and Technology, Hengyang 421001, China

<sup>4</sup>School of Fundamental Physics and Mathematical Sciences, Hangzhou Institute for Advanced Study, University of Chinese Academy of Sciences, Hangzhou 310024, China

**Abstract:** We investigated geodesic motion and gravitational-wave signatures of charged black holes with scalar hair. Using the effective potential approach, we analyzed marginally bound orbits and innermost stable circular orbits, showing how their positions and energy thresholds are modified by the scalar hair parameter  $r_B$ . These results demonstrate the role of scalar hair in altering the boundary of stable motion. We further explored periodic orbits characterized by rational frequency ratios, labeled by the index  $(z, w, \nu)$ , and quantified how scalar hair affects their orbital energy and angular momentum. Based on these orbital properties, we computed gravitational waveforms from extreme mass-ratio inspirals where a stellar-mass compact object orbits a supermassive charged black hole with scalar hair. Using the numerical kludge method, we generated waveforms that exhibit clear zoom-whirl patterns with morphology visibly affected by  $r_B$ . Our results show that scalar hair leaves distinguishable imprints on waveforms, suggesting that future space-based detectors could probe deviations from classical black hole spacetimes through extreme mass-ratio inspiral observations.

**Keywords:** gravitational wave, black hole, periodic orbit

**DOI:** 10.1088/1674-1137/ae28eb

**CSTR:** 32044.14.ChinesePhysicsC.50035103

## I. INTRODUCTION

Black holes represent one of the most remarkable predictions of Einstein's general relativity, serving as natural laboratories for testing strong-field gravity. The advent of gravitational-wave astronomy has opened new observational windows into these compact objects. Ground-based detectors such as LIGO and Virgo have confirmed stellar-mass black hole coalescences, providing strong evidence for general relativity in the dynamical, strong-field regime [1–8]. Future space-based missions, including LISA [9], Taiji [10], TianQin [11], and DECIGO [12], will extend this frontier by targeting extreme mass-ratio inspirals (EMRIs), where stellar-mass compact objects spiral into supermassive black holes [13]. These systems are particularly valuable because the small companion traces intricate geodesics, mapping the spacetime of the central object with exquisite precision. Consequently, EMRIs offer unique probes of black hole structure and potential de-

viations from general relativity [14–16].

Orbital dynamics around black holes play crucial roles in both theoretical studies and astrophysical applications [17–21]. Among these, marginally bound orbits (MBOs) and innermost stable circular orbits (ISCOs) are particularly important: MBOs separate bound from unbound motion, while ISCOs define accretion disk inner edges and serve as key parameters in gravitational-wave modeling [22–23]. Beyond these fundamental orbits, periodic trajectories characterized by rational frequency ratios exhibit zoom-whirl dynamics, where particles alternate between near-circular whirls and extended excursions [17–18, 24–26]. Such orbits illuminate phase-space structures, connecting regular circular motion with chaotic scattering, and leave distinctive imprints on gravitational waveforms. Periodic orbit frameworks have been applied to various black hole spacetimes, including charged black holes [19], naked singularities [20], Einstein-Lovelock black holes [27], Kehagias-Sfetsos solu-

Received 5 November 2025; Accepted 4 December 2025; Accepted manuscript online 5 December 2025

\* This work was supported by the National Natural Science Foundation of China (Grants No. 12035005, No. 12547143, No. 12405055, and No. 12347111), the China Postdoctoral Science Foundation (Grant No. 2023M741148), the Postdoctoral Fellowship Program of CPSF (Grant No. GZC20240458), and the National Key Research and Development Program of China (Grant No. 2020YFC2201400)

† E-mail: tanqin@hunnu.edu.cn

‡ E-mail: jljing@hunnu.edu.cn

©2026 Chinese Physical Society and the Institute of High Energy Physics of the Chinese Academy of Sciences and the Institute of Modern Physics of the Chinese Academy of Sciences and IOP Publishing Ltd. All rights, including for text and data mining, AI training, and similar technologies, are reserved.

tions [28], quantum-corrected black holes [29], and brane-world black holes [30]; please, refer to [31–51] for further details. Collectively, studying MBOs, ISCOs, and periodic orbits provides a powerful framework for probing black hole geometries and testing general relativity [23].

Recently, Bah *et al.* introduced five-dimensional topological stars/black holes within Einstein-Maxwell theory [52–53]. This construction yields spacetimes smooth at microstate geometry levels while reproducing classical black hole properties macroscopically, enabling exploration of observational signatures. Previous studies investigated charged particle dynamics in this background [54–55]. Through Kaluza-Klein dimensional reduction, the five-dimensional Einstein-Maxwell theory maps to an effective four-dimensional Einstein-Maxwell-Dilaton theory admitting static, spherically symmetric solutions [56–57]. These solutions enable studies of observable phenomena including gravitational-wave emission, black hole shadows [58–64], and quasinormal modes [65–68], offering deeper insights into charged black hole properties.

In this study, we systematically investigated orbital dynamics in these backgrounds [22], including MBOs, ISCOs [23], and periodic orbit families characterized by rational frequency ratios. To connect theory with observation, we employed the numerical kludge approximation for computing EMRI waveforms around these black holes [69–77]. This method provides efficient waveform modeling: while not capturing full relativistic radiation structures, it reproduces main spectral features associated with orbital motion, including zoom-whirl dynamics. Thus, it serves as a useful tool for exploring how background geometry modifications, such as scalar hair presence, affect waveform morphology. We applied this method to generate representative signals from inspirals into charged black holes with scalar hair and analyze their spectral content.

The paper is organized as follows. In Section II, we overview charged black holes with scalar hair and derive the effective potential. In Section III, we analyze MBO and ISCO properties and their modification by  $r_B$ . In Section IV, we study the rational number  $q$  for periodic orbits and the impact of  $r_B$  on their energy and angular momentum. In Section V, we present gravitational waveforms from test objects on periodic orbits and their spectral properties. Finally, in Section VI, we provide a discussion and conclusions. Throughout, we use geometrized units with  $G = c = 1$ .

## II. CHARGED BLACK HOLES WITH SCALAR HAIR

We briefly review geodesic orbits around charged black holes with scalar hair. Starting from the five-dimen-

sional Einstein-Maxwell theory, the spherically symmetric metric ansatz is [55]

$$ds^2 = -f_S(r)dt^2 + f_B(r)dy^2 + \frac{1}{f_S(r)f_B(r)}dr^2 + r^2d\theta^2 + r^2\sin^2\theta d\phi^2, \quad (1)$$

with

$$f_B(r) = 1 - \frac{r_B}{r}, \quad (2)$$

$$f_S(r) = 1 - \frac{r_S}{r}. \quad (3)$$

This geometry exhibits two coordinate singularities: at  $r = r_S$  (event horizon) and  $r = r_B$  (where the  $y$ -circle shrinks to zero size, signaling spacetime termination). Bah *et al.* showed that, after coordinate redefinitions,  $r = r_B$  actually hosts a smooth bubble [56–57]. For  $r_S \geq r_B$ , the bubble lies inside the horizon, forming a black string configuration. For  $r_S < r_B$ , no horizon is encountered given that spacetime caps off smoothly at the bubble, interpreted as a topological star [56–57]. The metric (1) can be rewritten as

$$ds_5^2 = e^{2\Phi} ds_4^2 + e^{-4\Phi} dy^2, \quad (4)$$

$$ds_4^2 = f_B^{\frac{1}{2}} \left( -f_S dt^2 + \frac{dr^2}{f_B f_S} + r^2 d\theta^2 + r^2 \sin^2 \theta d\phi^2 \right), \quad (5)$$

where  $\Phi$  is a dilaton field with  $e^{2\Phi} = f_B^{-1/2}$ . We focus on the  $r_B < r_S$  case of the four-dimensional metric, corresponding to charged black holes with scalar hair.

Let us now analyze massive test particle orbits around this black hole. The test particle Lagrangian is [22]

$$\mathcal{L} = \frac{m}{2} g_{\mu\nu} \frac{dx^\mu}{d\tau} \frac{dx^\nu}{d\tau}, \quad (6)$$

where  $\tau$  and  $m$  denote proper time and test particle mass, respectively. We set  $m = 1$  for simplicity. The generalized momentum is

$$p_\mu = \frac{\partial \mathcal{L}}{\partial \dot{x}^\mu} = g_{\mu\nu} \dot{x}^\nu, \quad (7)$$

where overdots indicate proper time derivatives. The equations of motion are

$$p_t = f_B(r)^{\frac{1}{2}} f_S(r) \dot{t} = E, \\ p_r = \frac{\dot{r}}{f_B(r)^{\frac{1}{2}} f_S(r)}, \quad (8)$$

$$p_\theta = f_B(r)^{\frac{1}{2}} r^2 \dot{\theta}, \quad (9)$$

$$p_\phi = f_B(r)^{\frac{1}{2}} r^2 \sin^2 \theta \dot{\phi} = L, \quad (10)$$

where  $E$  and  $L$  represent energy and orbital angular momentum per unit mass, respectively. This yields

$$\dot{t} = \frac{E}{f_B(r)^{\frac{1}{2}} f_S(r)}, \quad (11)$$

$$\dot{\phi} = \frac{L}{f_B(r)^{\frac{1}{2}} r^2 \sin^2 \theta}. \quad (12)$$

Restricting to spherical backgrounds, we assume equatorial orbits with  $\theta = \pi/2$  and  $\dot{\theta} = 0$ . The Lagrangian in Eq. (6) becomes

$$-\frac{E^2}{f_B(r)^{\frac{1}{2}} f_S(r)} + \frac{L^2}{f_B(r)^{\frac{1}{2}} r^2} + \frac{\dot{r}^2}{f_B(r)^{\frac{1}{2}} f_S(r)} = -1, \quad (13)$$

and the radial effective potential is

$$V_{\text{eff}} = \left( \sqrt{f_B(r) + \frac{L^2}{r^2}} \right) f_S(r). \quad (14)$$

Figure 1 shows the effective potential behavior. Figure 1(a) demonstrates that, as the orbital angular momentum increases, the potential develops extrema, with minima and maxima corresponding to stable and unstable circular orbits, respectively. Figure 1(b) shows that the potential maximum rises as  $r_B$  decreases. As  $r \rightarrow +\infty$ ,  $V_{\text{eff}} \rightarrow 1$ , implying that  $E = 1$  serves as the critical energy separating bound from unbound motion, with bound trajectories satisfying  $E \leq 1$ .

The effective potential structure determines stable and unstable circular orbit locations, constraining allowed particle energies and angular momenta. For massive particles such as orbiting black holes, bound trajectories exist between MBOs and ISCOs, with energy confined to

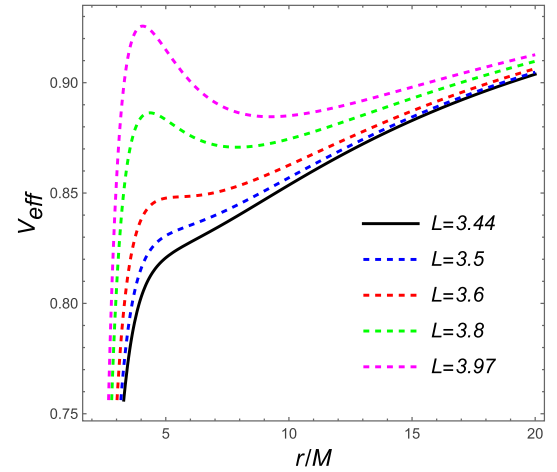
$$E_{\text{ISCO}} \leq E \leq E_{\text{MBO}} = 1. \quad (15)$$

Here,  $E_{\text{MBO}} = 1$  corresponds to particles having just enough energy to escape to infinity from the MBO, while  $E_{\text{ISCO}}$  represents ISCO energy; particles with lower energies inevitably fall into the black hole.

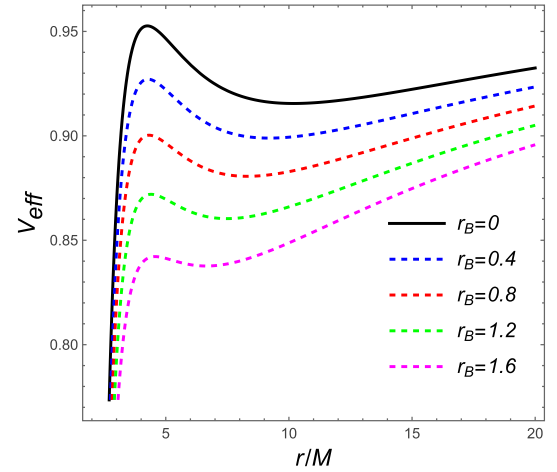
Similarly, the bound orbit angular momentum is restricted by

$$L \geq L_{\text{ISCO}}, \quad (16)$$

where  $L_{\text{ISCO}}$  denotes ISCO angular momentum. These ef-



(a)  $r_B = 1$



(b)  $L/M = 3.8$

**Fig. 1.** (color online) Effective potential (Eq. (14)) for test particle motion in charged black holes with scalar hair. (1a) Potential profiles for varying angular momentum at fixed  $r_B$ . (1b) Behavior for varying  $r_B$  at constant angular momentum.

fective potential features define the allowed bound motion phase space around charged black holes with scalar hair.

### III. MARGINALLY BOUND ORBIT AND INNERMOST STABLE CIRCULAR ORBIT

We focus on MBOs and ISCOs for massive test particles around charged black holes. The MBO corresponds to the minimum-radius circular orbit allowing gravitational binding, with particles having just sufficient energy to escape to infinity. For the effective potential  $V_{\text{eff}}$ , MBOs satisfy

$$V_{\text{eff}}(r_{\text{MBO}}) = 1, \quad (17)$$

$$\left. \frac{dV_{\text{eff}}}{dr} \right|_{r_{\text{MBO}}} = 0, \quad (18)$$

ensuring circular orbits without stability requirements.

The ISCO represents the smallest radius maintaining stable circular trajectories, determined by

$$V_{\text{eff}}(r_{\text{ISCO}}) = E^2, \quad (19)$$

$$\left. \frac{dV_{\text{eff}}}{dr} \right|_{r_{\text{ISCO}}} = 0, \quad (20)$$

$$\left. \frac{d^2V_{\text{eff}}}{dr^2} \right|_{r_{\text{ISCO}}} = 0, \quad (21)$$

where particles with sub-ISCO energies plunge into the black hole. These characteristic orbits define the radial range for bound circular motion around charged black holes with scalar hair.

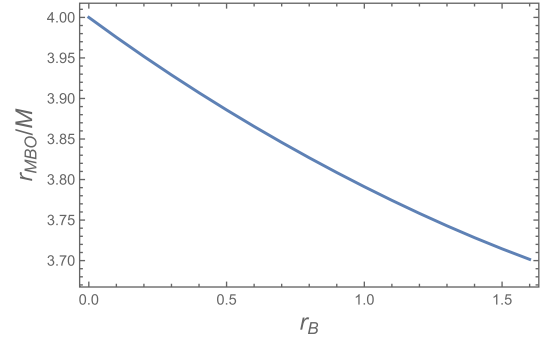
To determine MBO characteristics, we employ Eq. (17). The resulting high-order algebraic equations prevent closed-form solutions, so we solved it numerically. Figure 2 shows the MBO radius and angular momentum dependence on  $r_B$ . While the MBO radius decreases with increasing  $r_B$ , the associated angular momentum grows monotonically, indicating that scalar hair enables inward MBO shifts but requires larger angular momentum for marginal binding.

The ISCO, determined by Eq. (19), also depends on  $r_B$ . Numerical solutions yield ISCO radius, angular momentum, and energy variations with  $r_B$ , as shown in Fig. 3. ISCO radius and energy decrease with increasing  $r_B$ , while angular momentum increases, demonstrating that scalar hair pushes ISCOs inward and reduces stability energy thresholds but requires higher angular momentum for orbital stability.

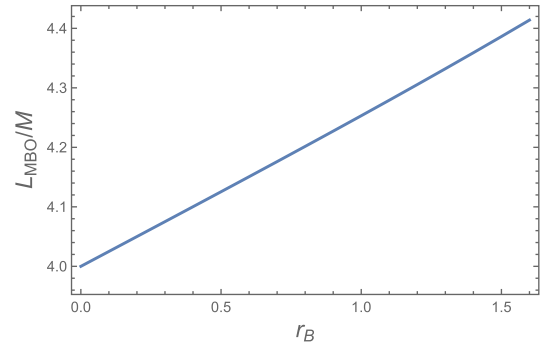
Finally, Fig. 4 shows admissible bound orbit parameter space in the  $(E, L)$  plane from Eqs. (15) and (16). For fixed angular momentum, larger  $r_B$  values extend the upper energy boundary, reflecting the enlargement of energetically allowed bound orbits of scalar hair, enriching orbital dynamics.

#### IV. PERIODIC ORBITS

Having examined MBOs and ISCOs, we now consider periodic orbits near charged black holes with scalar hair. These occur when azimuthal-to-radial frequency ratios become rational. While generally  $\omega_\phi/\omega_r$  is irrational, it can be approximated by nearby rational values, enabling understanding of generic trajectories through neighboring periodic ones and their gravitational wave signatures [17]. Fundamental orbital frequencies are rationally related, with each orbit indexed by  $(z, w, v)$  and



(a)



(b)

**Fig. 2.** (color online) MBO properties around charged black holes with scalar hair. (a) MBO radius versus  $r_B$ . (b) MBO angular momentum versus  $r_B$ . Radius decreases while angular momentum increases with  $r_B$ .

the following rational parameter:

$$q \equiv \frac{\omega_\phi}{\omega_r} - 1 = w + \frac{v}{z}, \quad (22)$$

where  $z$  (zoom),  $w$  (whirl), and  $v$  (vertex) are coprime integers. Using equations of motion (Eqs. (11)–(12) and (22)), this becomes

$$q = \frac{1}{\pi} \int_{r_2}^{r_1} \frac{L}{r^2 \sqrt{f_B(r)} \sqrt{E^2 - V_{\text{eff}}(r)}} dr - 1, \quad (23)$$

where  $r_1$  and  $r_2$  denote periapsis and apoapsis, respectively. Fixing angular momentum as

$$L = \frac{L_{\text{MBO}} + L_{\text{ISCO}}}{2}, \quad (24)$$

we can plot  $q$  versus orbital energy  $E$  for different  $r_B$  values. Similarly, fixing energy at  $E = 0.96$ , we can plot  $q$  versus angular momentum  $L$  for varying  $r_B$ , as shown in Fig. 5.

Figure 5 shows that  $q$  increases slowly with  $E$  initially but diverges as  $E$  approaches its maximum; with respect to  $L$ ,  $q$  diverges near minimal  $L$  and then gradually decreases. For fixed  $q$ , orbital energy  $E$  decreases while

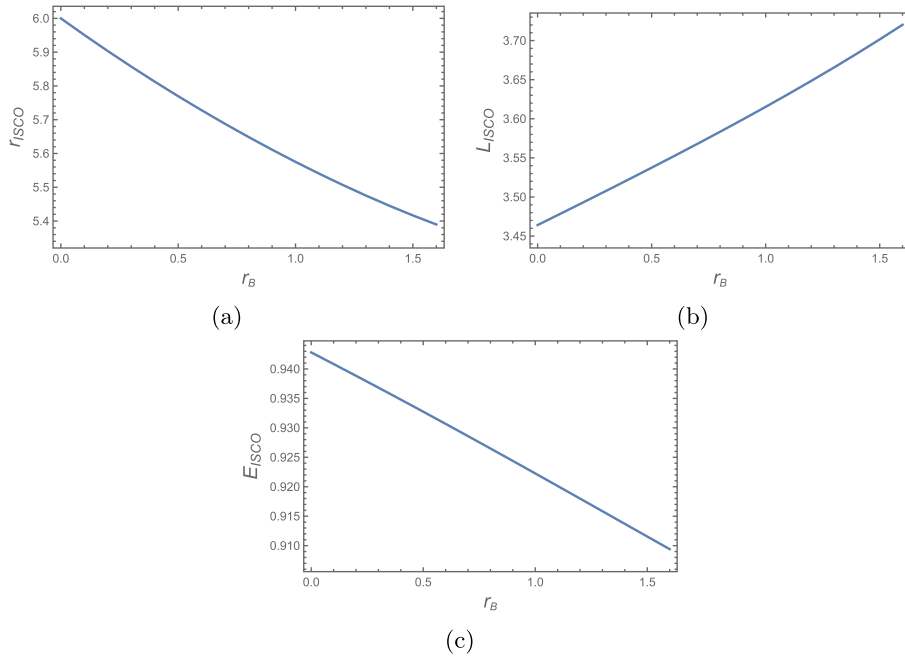


**Fig. 3.** (color online) Allowed bound orbit parameter space around charged black holes with scalar hair, showing orbital angular momentum versus energy for different  $r_B$  values.

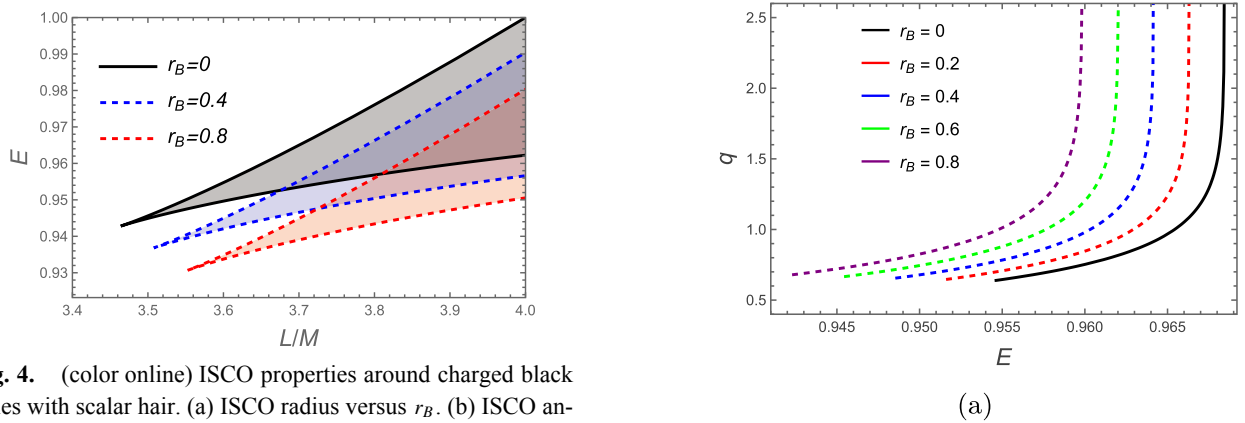


**Fig. 4.** (color online) ISCO properties around charged black holes with scalar hair. (a) ISCO radius versus  $r_B$ . (b) ISCO angular momentum versus  $r_B$ . (c) ISCO energy versus  $r_B$ . Radius and energy decrease while angular momentum increases with  $r_B$ .

angular momentum  $L$  increases with  $r_B$ ; consequently, the maximal orbital energy decreases with  $r_B$  while the minimal angular momentum increases. Although  $r_B$  is physically expected to be small, we adopted relatively large values to qualitatively analyze its influence on periodic orbits and associated gravitational-wave signatures.

For periodic orbits indexed by different  $(z, w, \nu)$  values around charged black holes with varying  $r_B$ , we numerically calculated orbital energy  $E$  with fixed  $L = (L_{\text{MBO}} + L_{\text{ISCO}})/2$  and angular momentum  $L$  with fixed  $E = 0.96$ . The results appear in Tables 1 and 2. The orbital energy decreases while the angular momentum increases with  $r_B$ .

Periodic orbits with different values of  $(z, w, \nu)$  around charged black holes with  $r_B = 0.6$  are shown in Figs. 6

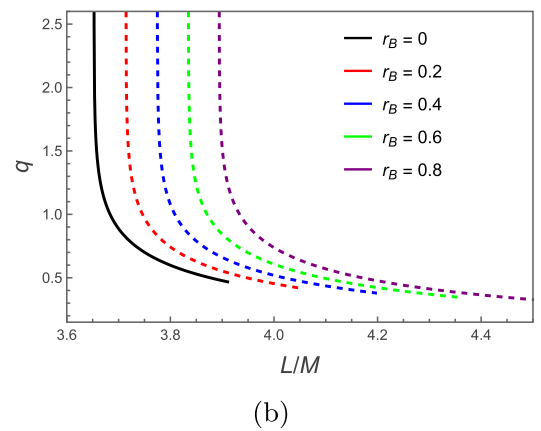


**Fig. 5.** (color online) (a) Rational number  $q$  versus periodic orbit energy for different  $r_B$ , with fixed  $L = (L_{\text{MBO}} + L_{\text{ISCO}})/2$ . (b)  $q$  versus angular momentum for different  $r_B$ , with fixed  $E = 0.96$ .

**Table 1.** Energy  $E$  for periodic orbits with different values of  $(z, w, v)$  and  $r_B$ , with fixed  $L = (L_{\text{MBO}} + L_{\text{ISCO}})/2$ .

$r_B$	$E_{(1,1,0)}$	$E_{(1,2,0)}$	$E_{(2,1,1)}$	$E_{(2,2,1)}$	$E_{(3,1,2)}$	$E_{(3,2,2)}$	$E_{(4,1,3)}$	$E_{(4,2,3)}$
0	0.96542525	0.96838267	0.96802639	0.96843422	0.96822477	0.96843840	0.96828487	0.96843968
0.2	0.96293241	0.96625659	0.96584493	0.96631807	0.96607270	0.96632319	0.96614228	0.96632477
0.4	0.96032030	0.96408470	0.96360387	0.96415914	0.96386802	0.96416553	0.96394946	0.96416751
0.6	0.95763524	0.96192560	0.96135870	0.96201690	0.96166766	0.96202499	0.96176390	0.96202753
0.8	0.95478014	0.95970156	0.95902643	0.95981519	0.95939109	0.95982561	0.95950598	0.95982893

**Table 2.** Angular momentum  $L$  for periodic orbits with different values of  $(z, w, v)$  and  $r_B$ , with fixed  $E = 0.96$ .

$r_B$	$L_{(1,1,0)}/M$	$L_{(1,2,0)}/M$	$L_{(2,1,1)}/M$	$L_{(2,2,1)}/M$	$L_{(3,1,2)}/M$	$L_{(3,2,2)}/M$	$L_{(4,1,3)}/M$	$L_{(4,2,3)}/M$
0	3.68358774	3.65340564	3.65759567	3.65270065	3.65533454	3.65263627	3.65462100	3.65261582
0.2	3.74626497	3.71506053	3.71933926	3.71435382	3.71702197	3.71429029	3.71629392	3.71427021
0.4	3.80857799	3.77564975	3.78016415	3.77490609	3.77771822	3.77483941	3.77695010	3.77481836
0.6	3.87092194	3.83556164	3.84045847	3.83474663	3.83781119	3.83467297	3.83697747	3.83464965
0.8	3.93368898	3.89514037	3.90058032	3.89421534	3.89765254	3.89413033	3.89672527	3.89410326

and 7 with either fixed  $E = 0.96$  or  $L = (L_{\text{MBO}} + L_{\text{ISCO}})/2$ . Orbits with larger zoom numbers  $z$  exhibit more intricate structures, while those with larger whirl numbers  $w$  undergo more revolutions between successive apoapses.

## V. NUMERICAL KLUDGE GRAVITATIONAL WAVEFORMS FROM PERIODIC ORBITS

A stellar-mass compact object on a periodic trajectory around a charged black hole with scalar hair constitutes an extreme mass-ratio inspiral (EMRI) system. Gravitational radiation from such systems potentially carries imprints of both periodic orbital structure and central black hole information. Standard EMRI waveform evaluation is based on the adiabatic approximation [78–86]. Given that secondary orbital parameters evolve over time scales much longer than orbital periods, motion approximates geodesics with nearly constant energy and angular momentum over multiple cycles, neglecting radiation reaction in short intervals. Therefore, we computed gravitational waveforms during one complete orbital cycle.

We adopted the numerical kludge framework, effective for modeling EMRI waveforms [69]. Specifically, we numerically integrated equations of motion (Eq. (8)) to obtain small body trajectories, which were inserted into the quadrupole radiation formula [85–86] to generate waveforms. For a mass  $m$  particle, the symmetric trace-free (STF) mass quadrupole moment is

$$I^{ij} = \left[ \int_{\text{STF}} d^3x x^i x^j T^{tt}(t, x^i) \right], \quad (25)$$

with point particle stress-energy tensor on worldline  $Z^i(t)$  given by

$$T^{tt}(t, x^i) = m \delta^3(x^i - Z^i(t)). \quad (26)$$

Following Refs. [39, 69], we interpret Boyer-Lindquist coordinates as effective spherical polar coordinates, projecting trajectories to Cartesian form via

$$x = r \sin \theta \cos \phi, \quad (27)$$

$$y = r \sin \theta \sin \phi, \quad (28)$$

$$z = r \cos \theta. \quad (29)$$

From Eqs. (25)–(11), metric perturbations describing gravitational-wave strain become

$$h_{ij} = \frac{2}{D_L} \frac{d^2 I_{ij}}{dt^2} = \frac{2m}{D_L} (a_i x_j + a_j x_i + 2v_i v_j), \quad (30)$$

where  $D_L$  is the luminosity distance, and  $v_i$  and  $a_i$  are spatial velocity and acceleration. To relate perturbations to detector response, we introduce a detector-adapted frame  $(X, Y, Z)$  [86], centered on the supermassive black hole and aligned as

$$\mathbf{e}_X = [\cos \zeta, -\sin \zeta, 0], \quad (31)$$

$$\mathbf{e}_Y = [\sin \iota \sin \zeta, -\cos \iota \cos \zeta, -\sin \iota], \quad (32)$$

$$\mathbf{e}_Z = [\sin \iota \sin \zeta, -\sin \iota \cos \zeta, \cos \iota], \quad (33)$$

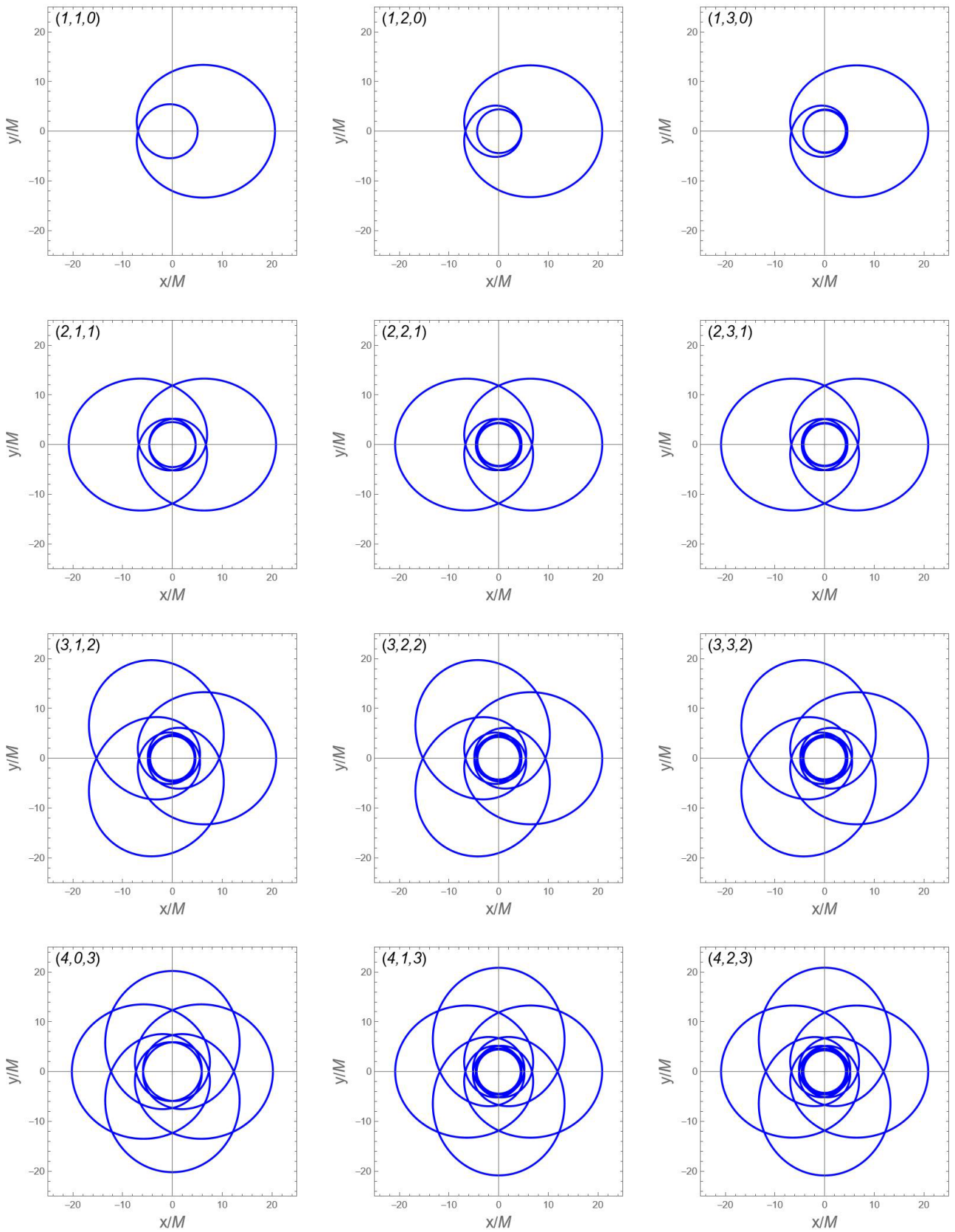


**Fig. 6.** (color online) Periodic orbits with different values of  $(z, w, v)$  around charged black holes with scalar hair, for  $r_B = 0.6$  and  $E = 0.96$ .

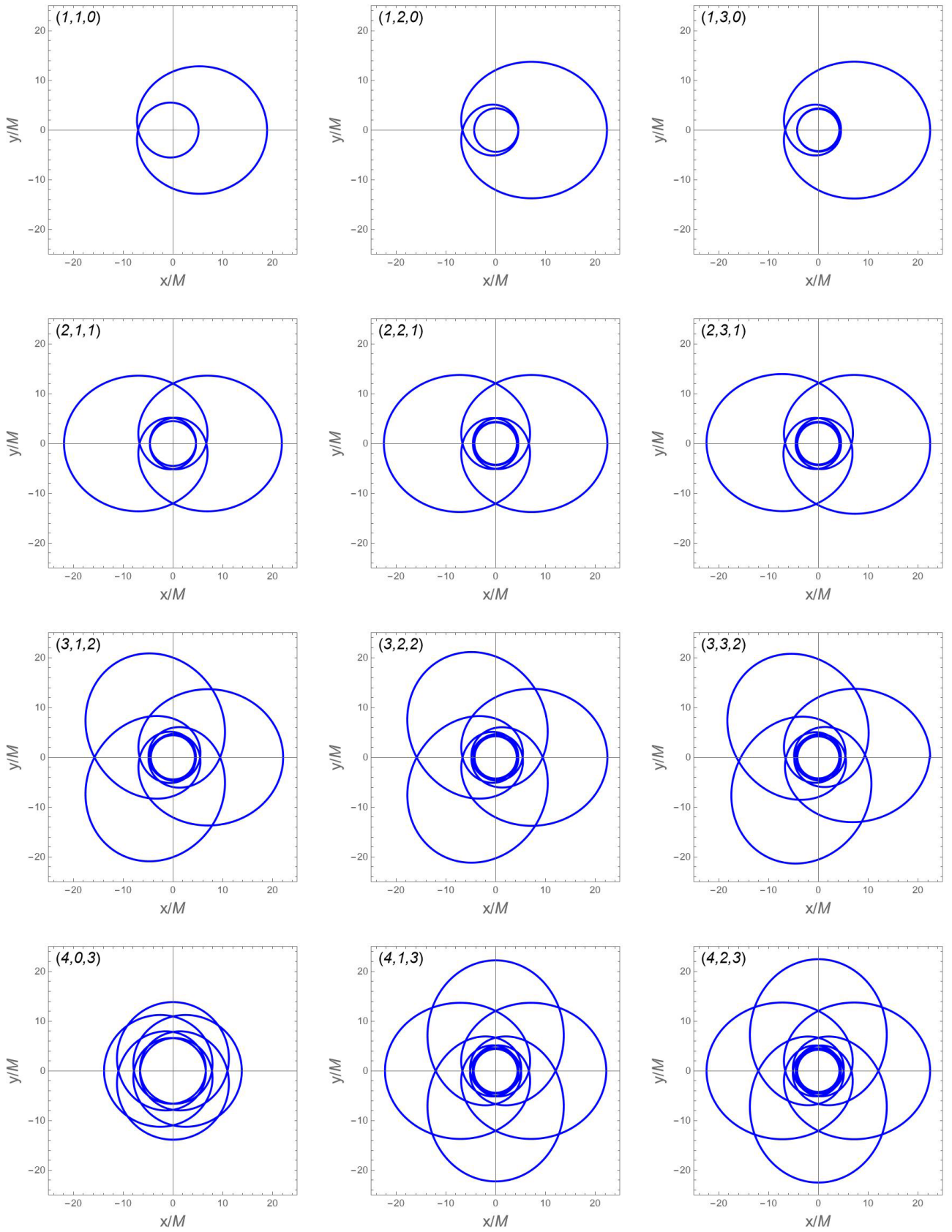


**Fig. 7.** (color online) Periodic orbits with different values of  $(z, w, v)$  around charged black holes with scalar hair, for  $r_B = 0.6$  and  $L = \frac{(L_{\text{MBO}} + L_{\text{ISCO}})}{2}$ .

where  $\iota$  is the orbital plane inclination relative to the  $X$ - $Y$  plane, and  $\zeta$  is pericenter longitude. In this frame, the two gravitational-wave polarizations are

$$h_+ = \frac{1}{2}(e_X^i e_X^j - e_Y^i e_Y^j)h_{ij}, \quad (34)$$

$$h_\times = \frac{1}{2}(e_X^i e_Y^j + e_Y^i e_X^j)h_{ij}, \quad (35)$$

yielding

$$h_+ = \frac{1}{2}(h_{\zeta\zeta} - h_u), \quad (36)$$

$$h_\times = h_{u\zeta}, \quad (37)$$

with components [69]

$$h_{\zeta\zeta} = h_{xx} \cos^2 \zeta - h_{xy} \sin 2\zeta + h_{yy} \sin^2 \zeta, \quad (38)$$

$$\begin{aligned} h_u &= \cos^2 \iota [h_{xx} \sin^2 \zeta + h_{xy} \sin 2\zeta + h_{yy} \cos^2 \zeta] + h_{zz} \sin^2 \iota \\ &\quad - \sin 2\iota [h_{xz} \sin \zeta + h_{yz} \cos \zeta], \\ h_{u\zeta} &= \cos \iota \left( \frac{1}{2} h_{xx} \sin 2\zeta + h_{xy} \cos 2\zeta - \frac{1}{2} h_{yy} \sin 2\zeta \right) \\ &\quad + \sin \iota [h_{yz} \sin \zeta - h_{xz} \cos \zeta]. \end{aligned} \quad (39)$$

As a concrete example, consider an EMRI with an  $m = 10M_\odot$  stellar-mass object orbiting a  $M = 10^6 M_\odot$  charged black hole with scalar hair at  $D_L = 2$  Gpc. For  $\iota = \pi/4$ ,  $\zeta = \pi/4$ , and  $r_B = 0.6$ , the corresponding polarizations are shown in Fig. 8. Note that the waveforms exhibit alternating zoom and whirl phases within single orbits, reflecting underlying periodic trajectory dynamics. Orbits with higher zoom indices  $z$  produce more intricate waveform substructures, corresponding to multi-leaf orbital morphology.

Under identical setup, Fig. 9 compares waveforms from fixed (3,2,2) periodic orbits for varying  $r_B$ . Increasing  $r_B$  modestly modifies the waveform amplitude while inducing cumulative phase advancement. This phase shift builds gradually over time, becoming increasingly significant during orbital evolution.

## VI. CONCLUSIONS AND OUTLOOK

In this study, we systematically investigated geodesic

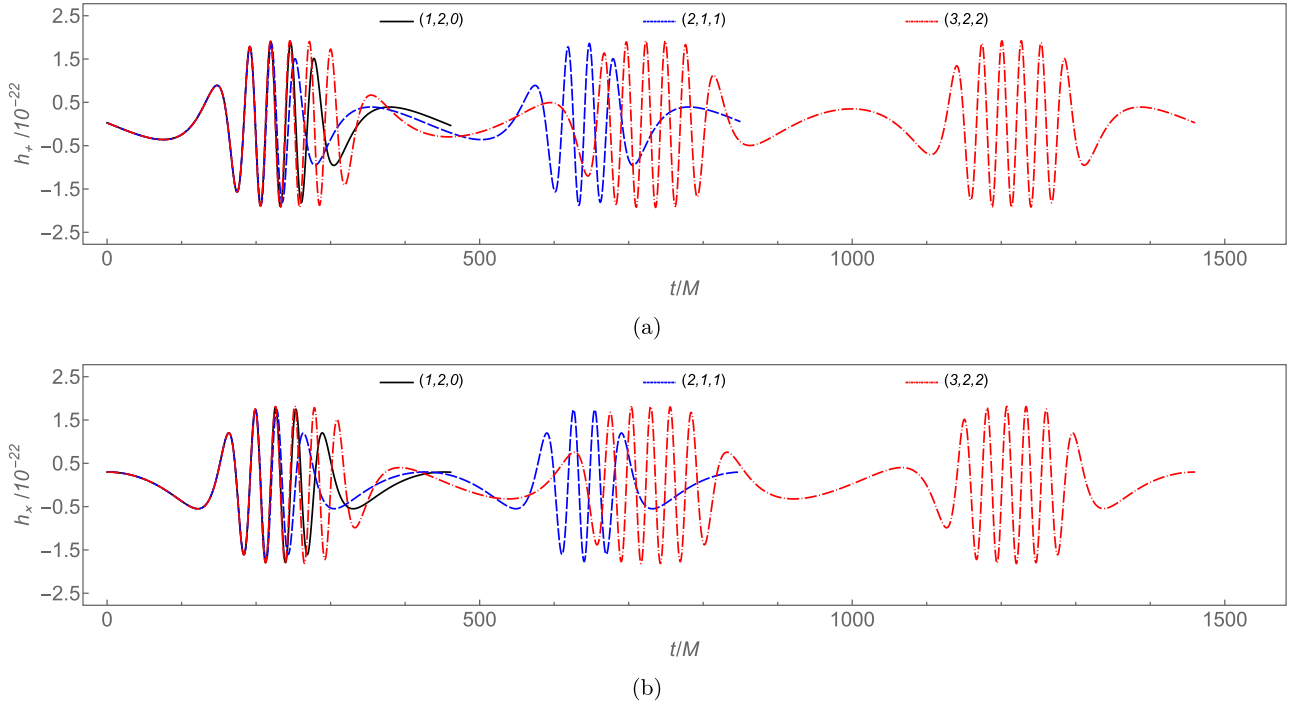


**Fig. 8.** (color online) Gravitational waveforms from  $m = 10M_\odot$  test objects on different periodic orbits around  $M = 10^6 M_\odot$  supermassive charged black holes with scalar hair, with fixed  $E = 0.96$ .

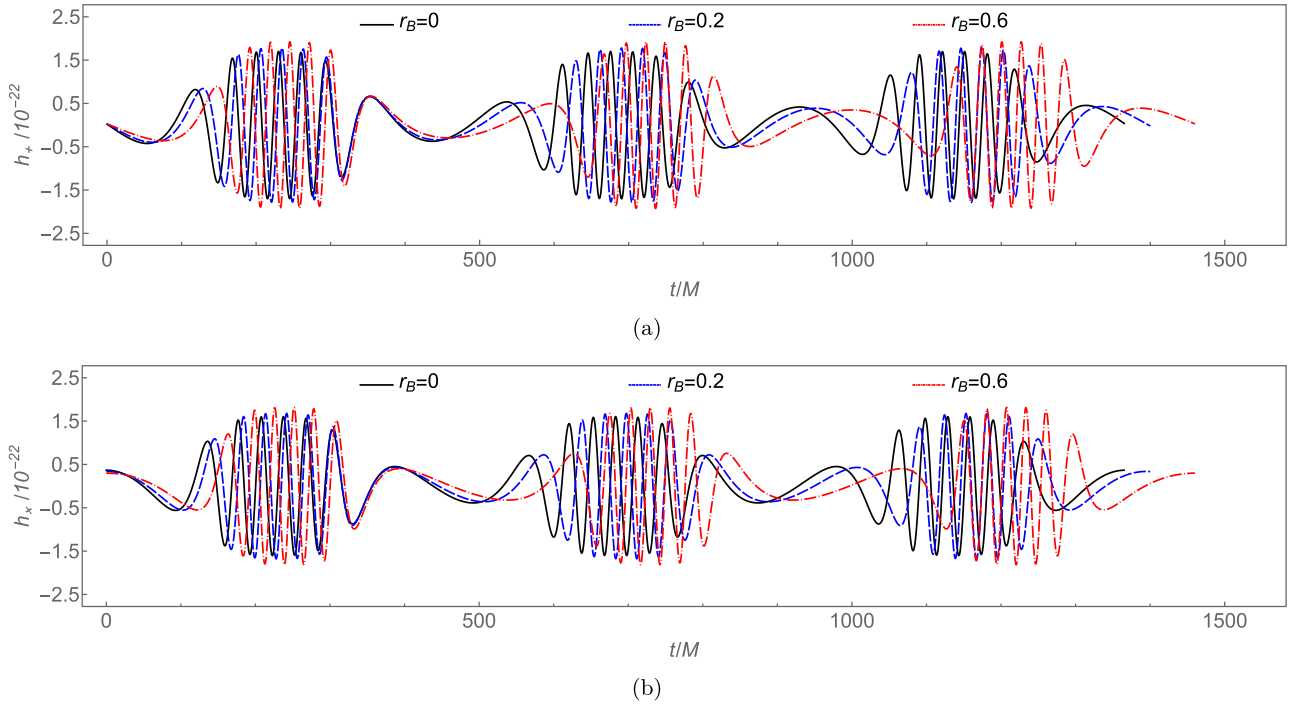


**Fig. 9.** (color online) Gravitational waveforms from  $m = 10M_\odot$  test objects on  $(3, 2, 2)$  periodic orbits around  $M = 10^6 M_\odot$  supermassive charged black holes with scalar hair, for different  $r_B$ , with fixed  $E = 0.96$ .

motion and associated gravitational wave signatures in charged black hole spacetimes with scalar hair. Using the effective potential approach, we analyzed marginally bound orbits (MBOs) and innermost stable circular orbits (ISCOs). The results indicate that the scalar hair parameter  $r_B$  plays a significant role: increasing  $r_B$  shifts both MBOs and ISCOs inward, decreases corresponding orbital energies, and increases angular momenta required for stable motion. Consequently, the allowed bound orbit range in the  $(E, L)$  parameter space effectively extends.

We further conducted detailed studies of periodic orbits characterized by rational winding numbers and classified by integer indices  $(z, w, \nu)$ . The conducted analysis shows that increasing  $r_B$  generally reduces energies and raises angular momenta across different  $(z, w, \nu)$  combinations, highlighting the universal influence of scalar hair on orbital stability and underlying dynamical structure. Moreover, orbits with larger zoom or whirl numbers exhibit increasingly intricate geometrical features, including multiple near-horizon revolutions followed by rapid excursions, forming characteristic zoom-whirl behavior. These findings demonstrate that scalar hair not only modifies periodic orbit distribution in energy-angular momentum space but also significantly impacts morphological characteristics, revealing rich nonlinear dynamics in such spacetimes.

Building on this, we simulated gravitational waveforms from extreme mass-ratio inspirals (EMRIs) where stellar-mass compact objects move along periodic orbits around supermassive charged black holes with scalar hair. Numerical approximations reveal clear zoom-whirl signatures in waveforms, directly corresponding to underlying orbital geometry. Notably,  $r_B$  variations induce observable modifications in both waveform amplitude and phase, with cumulative phase shifts becoming increasingly significant during inspiral. These results underscore the potential of gravitational-wave astronomy—particularly future space-based detectors such as LISA—to probe deviations from Kerr black holes and constrain the presence of scalar hair in astrophysical black holes.

Looking ahead, several avenues merit investigation. Incorporating radiation reaction and full self-force corrections would enable more precise long-term EMRI evolution modeling. Extending analysis to rotating or non-equatorial orbits could further enrich waveform phenomenology. Finally, confronting predictions with actual detector sensitivity will be essential for assessing the feasibility of testing alternative black hole models and potential extra-dimensional effects through gravitational-wave observations.

## References

- [1] B. P. Abbott *et al.* (LIGO Scientific, Virgo), *Phys. Rev. Lett.* **116**, 061102 (2016), arXiv: 1602.03837[gr-qc]
- [2] B. P. Abbott *et al.* (LIGO Scientific, Virgo), *Phys. Rev. D* **93**, 122003 (2016), arXiv: 1602.03839[gr-qc]
- [3] B. P. Abbott *et al.* (LIGO Scientific, Virgo), *Phys. Rev. Lett.* **116**, 241102 (2016), arXiv: 1602.03840[gr-qc]
- [4] B. P. Abbott *et al.* (LIGO Scientific, Virgo), *Phys. Rev. Lett.* **116**, 131103 (2016), arXiv: 1602.03838[gr-qc]
- [5] B. P. Abbott *et al.* (LIGO Scientific, VIRGO), *Phys. Rev. Lett.* **118**, 221101 (2017), [Erratum: *Phys.Rev.Lett.* 121, 129901 (2018)], arXiv: 1706.01812[gr-qc]
- [6] B. P. Abbott *et al.* (LIGO Scientific, Virgo), *Astrophys. J. Lett.* **851**, L35 (2017), arXiv: 1711.05578[astro-ph.HE]
- [7] B. P. Abbott *et al.* (LIGO Scientific, Virgo), *Phys. Rev. Lett.* **119**, 141101 (2017), arXiv: 1709.09660[gr-qc]
- [8] B. P. Abbott *et al.* (LIGO Scientific, Virgo), *Phys. Rev. X* **9**, 031040 (2019), arXiv: 1811.12907[astro-ph.HE]
- [9] P. Amaro-Seoane *et al.* (LISA Collaboration), arXiv: 1702.00786 [astro-ph.IM]
- [10] W. R. Hu and Y. L. Wu, *Natl. Sci. Rev.* **4**, 685 (2017)
- [11] J. Luo *et al.* (TianQin Collaboration), *Class. Quant. Grav.* **33**, 035010 (2016), arXiv: 1512.02076[astro-ph.IM]
- [12] M. Musha (DECIGO Working group), *Proc. SPIE Int. Soc. Opt. Eng.* **10562**, 105623T (2017)
- [13] S. A. Hughes, *Class. Quant. Grav.* **18**, 4067 (2001), arXiv: gr-qc/0008058
- [14] K. Glampedakis, *Class. Quant. Grav.* **22**, S605 (2005), arXiv: gr-qc/0509024
- [15] E. Barausse, E. Berti, T. Hertog *et al.*, *Gen. Rel. Grav.* **52**, 81 (2020), arXiv: 2001.09793[gr-qc]
- [16] P. A. Seoane *et al.* (LISA Collaboration), *Living Rev. Rel.* **26**, 2 (2023), arXiv: 2203.06016[gr-qc]
- [17] J. Levin and G. Perez-Giz, *Phys. Rev. D* **77**, 103005 (2008), arXiv: 0802.0459[gr-qc]
- [18] J. Levin, *Class. Quant. Grav.* **26**, 235010 (2009), arXiv: 0907.5195[gr-qc]
- [19] V. Misra and J. Levin, *Phys. Rev. D* **82**, 083001 (2010), arXiv: 1007.2699[gr-qc]
- [20] G. Z. Babar, A. Z. Babar, and Y. K. Lim, *Phys. Rev. D* **96**, 084052 (2017), arXiv: 1710.09581[gr-qc]
- [21] Q. Tan, W. Deng, S. Long *et al.*, *JCAP* **05**, 044 (2025), arXiv: 2409.17760[gr-qc]
- [22] S. Chandrasekhar, *The mathematical theory of black holes*, (Oxford university press, 1998).
- [23] C. W. Misner, K. S. Thorne, and J. A. Wheeler, *Gravitation*, (New York: W. H. Freeman, 1973).
- [24] J. Levin and B. Grossman, *Phys. Rev. D* **79**, 043016 (2009), arXiv: 0809.3838[gr-qc]
- [25] S. Albanesi, A. Nagar, and S. Bernuzzi, *Phys. Rev. D* **104**, 024067 (2021), arXiv: 2104.10559[gr-qc]
- [26] R. Gold and B. Bruegmann, *Class. Quant. Grav.* **27**, 084035 (2010), arXiv: 0911.3862[gr-qc]
- [27] H. Y. Lin and X. M. Deng, *Phys. Dark Univ.* **31**, 100745 (2021)
- [28] S. W. Wei, J. Yang, and Y. X. Liu, *Phys. Rev. D* **99**, 104016 (2019), arXiv: 1904.03129[gr-qc]
- [29] X. M. Deng, *Phys. Dark Univ.* **30**, 100629 (2020)
- [30] X. M. Deng, *Eur. Phys. J. C* **80**, 489 (2020)
- [31] H. Y. Lin and X. M. Deng, *Eur. Phys. J. Plus* **137**, 176 (2022)
- [32] J. Zhang and Y. Xie, *Astrophys. Space Sci.* **367**, 17 (2022)
- [33] R. Wang, F. Gao, and H. Chen, *Annals Phys.* **447**, 169167 (2022)
- [34] J. T. Yao and X. Li, *Phys. Rev. D* **108**, 084067 (2023)
- [35] H. Y. Lin and X. M. Deng, *Eur. Phys. J. C* **83**, 311 (2023)
- [36] Z. Y. Tu, T. Zhu, and A. Wang, *Phys. Rev. D* **108**, 024035 (2023), arXiv: 2304.14160[gr-qc]
- [37] H. Jiang, M. Alloquolov, Q. Wu *et al.*, *Phys. Dark Univ.* **46**, 101627 (2024)
- [38] Y. Z. Li, X. M. Kuang, and Y. Sang, *Eur. Phys. J. C* **84**, 529 (2024), arXiv: 2401.16071[gr-qc]
- [39] S. Yang, Y. P. Zhang, T. Zhu *et al.*, *JCAP* **01**, 091 (2025), arXiv: 2407.00283[gr-qc]
- [40] L. Zhao, M. Tang, and Z. Xu, *Eur. Phys. J. C* **85**, 36 (2025), arXiv: 2411.01979[gr-qc]
- [41] E. L. B. Junior, J. T. S. S. Junior, F. S. N. Lobo *et al.*, *Eur. Phys. J. C* **85**, 557 (2025), arXiv: 2412.00769[gr-qc]
- [42] H. Gong, S. Long, X. J. Wang *et al.*, arXiv: 2509.23318[gr-qc]
- [43] C. H. Wang, X. C. Meng, Y. P. Zhang *et al.*, *JCAP*, **07**, 021 (2025), arXiv: 2502.08994[gr-qc]
- [44] C. H. Wang, Y. P. Zhang, T. Zhu *et al.*, arXiv: 2508.20558[gr-qc]
- [45] M. Alloquolov, S. Shaymatov, B. Ahmedov *et al.*, arXiv: 2508.05245 [gr-qc]
- [46] M. Alloquolov, T. Xamidov, S. Shaymatov *et al.*, *Eur. Phys. J. C* **85**, 798 (2025), arXiv: 2504.05236[gr-qc]
- [47] Y. Ravanal, G. Gómez, and N. Cruz, *Phys. Rev. D* **110**, 023027 (2024), arXiv: 2404.06774[astro-ph.CO]
- [48] Y. Ravanal, G. Gómez, and N. Cruz, *Phys. Rev. D* **108**, 083004 (2023), arXiv: 2306.10204[astro-ph.CO]
- [49] E. Battista and V. De Falco, *Eur. Phys. J. C* **82**, 782 (2022), arXiv: 2208.09839[gr-qc]
- [50] E. Battista and V. De Falco, *Eur. Phys. J. C* **82**, 628 (2022), arXiv: 2206.12907[gr-qc]
- [51] E. Battista and V. De Falco, *Phys. Rev. D* **104**, 084067 (2021), arXiv: 2109.01384[gr-qc]
- [52] I. Bah and P. Heidmann, *Phys. Rev. Lett.* **126**, 151101 (2021), arXiv: 2011.08851[hep-th]
- [53] I. Bah and P. Heidmann, *JHEP* **09**, 147 (2021), arXiv: 2012.13407[hep-th]
- [54] S. Stotyn and R. B. Mann, *Phys. Lett. B* **705**, 269 (2011), arXiv: 1105.1854[hep-th]
- [55] Y.-K. Lim, *Phys. Rev. D* **103**, 084044 (2021), arXiv: 2102.08531[gr-qc]
- [56] I. Bena and D. R. Mayerson, *Phys. Rev. Lett.* **125**, 221602 (2020), arXiv: 2006.10750[hep-th]
- [57] I. Bena and D. R. Mayerson, *JHEP* **03**, 114 (2021), arXiv: 2007.09152[hep-th]
- [58] W. D. Guo, S. W. Wei, and Y. X. Liu, *Eur. Phys. J. C* **83**, 197 (2023), arXiv: 2203.13477[gr-qc]
- [59] C. Chen, Q. Pan, and J. Jing, *JCAP* **08**, 043 (2025), arXiv: 2410.09022[gr-qc]
- [60] W. T. Liu, D. Wu, X. J. Fang *et al.*, *JCAP* **08**, 035 (2024), arXiv: 2406.00579[gr-qc]
- [61] Z. Zhang, S. Chen, and J. Jing, *JCAP* **09**, 027 (2024), arXiv: 2404.12223[gr-qc]
- [62] S. Chen and J. Jing, *JCAP* **05**, 023 (2024), arXiv: 2310.06490[gr-qc]
- [63] S. Zare, L. M. Nieto, X. H. Feng *et al.*, *JCAP* **08**, 041 (2024), arXiv: 2406.07300[astro-ph.HE]
- [64] W. T. Liu, D. Wu, and J. Wang, *Phys. Lett. B* **858**, 139052 (2024), arXiv: 2408.05569[gr-qc]
- [65] W. D. Guo, Q. Tan, and Y. X. Liu, *Phys. Rev. D* **107**,

- 124046 (2023), arXiv: 2212.08784[gr-qc]
- [66] W. D. Guo and Q. Tan, *Universe* **9**, 320 (2023), arXiv: 2402.14265[gr-qc]
- [67] W. T. Liu, X. J. Fang, J. L. Jing *et al.*, *JCAP* **11**, 057 (2023), arXiv: 2306.03599[gr-qc]
- [68] W. T. Liu, X. J. Fang, J. L. Jing, *Eur. Phys. J. C* **83**, 83 (2023), arXiv: 2211.03156[gr-qc]
- [69] S. Babak, H. Fang, J. R. Gair *et al.*, *Phys. Rev. D* **75**, 024005 (2007), [Erratum: *Phys. Rev. D* **77**, 04990 (2008)], arXiv: gr-qc/0607007
- [70] J. Jing, S. Long, W. Deng *et al.*, *Sci. China Phys. Mech. Astron.* **68**, 120411 (2025), arXiv: 2509.06448[gr-qc]
- [71] X. Qiao, Z. W. Xia, Q. Pan *et al.*, *JCAP* **03**, 006 (2025), arXiv: 2408.10022[gr-qc]
- [72] W. Deng, S. Long, and J. Jing, *Sci. China Phys. Mech. Astron.* **67**, 290412 (2024), arXiv: 2405.16423[gr-qc]
- [73] S. Long, W. Deng, and J. Jing, *Sci. China Phys. Mech. Astron.* **67**, 260412 (2024), arXiv: 2403.09211[gr-qc]
- [74] C. Chen and J. Jing, *Sci. China Phys. Mech. Astron.* **67**, 110411 (2024), arXiv: 2311.15295[gr-qc]
- [75] J. L. Jing, W. K. Deng, S. Long *et al.*, *Eur. Phys. J. C* **83**, 608 (2023) [Erratum: *Eur. Phys. J. C* **83**, 712 (2023)], arXiv: 2307.05971[gr-qc]
- [76] J. Jing, W. Deng, S. Long *et al.*, *Sci. China Phys. Mech. Astron.* **66**, 270411 (2023), arXiv: 2305.03225[gr-qc]
- [77] M. S. Delos, A. Rantala, S. Young *et al.*, *JCAP* **12**, 005 (2024), arXiv: 2410.01876[astro-ph.CO]
- [78] S. A. Hughes, *Phys. Rev. D* **61**, 084004 (2000) [Erratum: *Phys. Rev. D* **63**, 049902 (2001), Erratum: *Phys. Rev. D* **65**, 069902 (2002), Erratum: *Phys. Rev. D* **67**, 089901 (2003), Erratum: *Phys. Rev. D* **78**, 109902 (2008), Erratum: *Phys. Rev. D* **90**, 109904 (2014)], arXiv: gr-qc/9910091
- [79] S. A. Hughes, S. Drasco, E. E. Flanagan *et al.*, *Phys. Rev. Lett.* **94**, 221101 (2005), arXiv: gr-qc/0504015
- [80] S. Drasco, E. E. Flanagan, and S. A. Hughes, *Class. Quant. Grav.* **22**, S801 (2005), arXiv: gr-qc/0505075
- [81] P. A. Sundararajan, G. Khanna, and S. A. Hughes, *Phys. Rev. D* **76**, 104005 (2007), arXiv: gr-qc/0703028
- [82] E. Poisson and C. M. Will, *Gravity: Newtonian, postnewtonian, relativistic*, (Cambridge: Cambridge University Press, 2014).
- [83] P. A. Sundararajan, G. Khanna, S. A. Hughes *et al.*, *Phys. Rev. D* **78**, 024022 (2008), arXiv: 0803.0317[gr-qc]
- [84] K. S. Thorne, *Rev. Mod. Phys.* **52**, 299 (1980)
- [85] J. Miller and A. Pound, *Phys. Rev. D* **103**, 064048 (2021), arXiv: 2006.11263[gr-qc]
- [86] S. Isoyama, R. Fujita, A. J. K. Chua *et al.*, *Phys. Rev. Lett.* **128**, 231101 (2022), arXiv: 2111.05288[gr-qc]